ACADEMIC PRESS

Available online at www.sciencedirect.com

SCIENCE DIRECT®

Icarus 161 (2003) 47–65

ICARUS

www.elsevier.com/locate/icarus

Multiple emission angle surface–atmosphere separations of Thermal Emission Spectrometer data

Joshua L. Bandfield[a,*] and Michael D. Smith[b]

[a] *Department of Geological Sciences, Arizona State University, Tempe, AZ 85287-6305, USA*
[b] *NASA Goddard Space Flight Center, Greenbelt, MD 20771, USA*

Received 10 June 2002; revised 30 August 2002

Abstract

A method for separating the spectral signatures of the Martian surface and atmosphere was developed and is applied to multiple emission angle data returned from the MGS TES instrument. This method includes correlated-*k* and index gas removal algorithms that may be applied to all nadir-pointing TES data. Initial results have provided new and refined measurements of the spectral shapes of atmospheric dust and the Martian surface. Surface temperatures and atmospheric dust opacities are also retrieved with improved accuracy over single observation temperature and opacity retrievals. Low-albedo surfaces display absorptions consistent in both shape and depth with previous studies. These surfaces may be closely modeled using a combination of previously derived basalt, andesitic, and high-albedo surface spectral shapes. Short wavelengths display no significant absorptions, indicating both the coarse particulate nature of the surface and the lack of significant amounts of carbonate. Moderate- and high-albedo surfaces have spectral shapes distinctive of fine particulate silicate materials. No single material can match the entire high-albedo surface spectrum, though there are clear indications of a material that closely matches intermediate to calcic plagioclase and an emission peak at $\sim$1620 cm^{-1} due to bound water. The lack of residual restrahlen silicate absorptions indicates that minerals such as olivine or pyroxene are not present in high-albedo surfaces at significant (but unknown) abundances. High-albedo surface results presented here are in agreement with and complementary to shorter wavelength observations. The Martian dust is composed of both primary and secondary minerals. Either chemical weathering has not completely altered its source material or the soil is a mixture of altered and unaltered sources. Further laboratory studies are needed to better establish detection limits and behavior of mineral mixtures of fine particulates in the thermal infrared portion of the spectrum.

I. Introduction

A. Usefulness of TIR measurements

The thermal infrared portion of the spectrum (roughly defined here as $\sim$5 to 50 μm or 200 to 2000 cm^{-1}) measures both the temperature-dependent emitted energy and compositional absorptions from both the surface and atmosphere of a planet. This allows the determination of surface and atmospheric compositions, surface temperature, thermal inertia, rock abundance, atmospheric temperature profiles, and atmospheric isotopic ratios. The large amount and wide variety of information that may be retrieved makes the thermal infrared an ideal spectral region with which to observe Mars.

This variety of information also presents the complicated problem of isolating each of the temperature and compositional parameters and determining their relative contribution to the measured radiance. Two basic surface–atmosphere separation algorithms have been developed (Smith et al., 2000a) based on the consistency of atmospheric spectral shapes (Bandfield et al., 2000a). These algorithms have allowed both surface emissivity and atmospheric dust and water ice opacity retrievals.

Atmospheric dust, water ice, water vapor, and CO_2 combine to form continuous absorptions throughout the thermal infrared portion of the Martian spectrum. These absorptions, particularly the atmospheric dust, make it difficult to discern whether or not significant absorptions are present on the

* Corresponding author. Fax: +1-480-965-1787.
E-mail address: joshband@asu.edu (J.L. Bandfield).

0019-1035/03/$ – see front matter © 2003 Elsevier Science (USA). All rights reserved.
PII: S0019-1035(02)00025-8

surface and impossible to accurately determine their shape without some form of atmospheric correction. The atmospheric absorptions can greatly exceed the magnitude of absorptions due to surface composition.

Alternately, surface spectral absorptions can cause overestimates of atmospheric dust opacities by a factor of greater than 2 during periods of low dust loading (Smith et al., 2000a) and accurate knowledge of the surface emissivity is necessary to retrieve accurate dust and water ice opacities from nadir pointing observations (Smith et al., 2000b). Accurate surface emissivities are also important for determining water ice and dust particle size distributions and compositions (Wolff et al., 2001; Snook, 2002).

This work presents an improved surface–atmosphere separation algorithm that uses observations of a surface from multiple emission angles. For measurements of a single surface through multiple emission angles, the path length through the atmosphere changes by a known amount and the contributions from the surface and the atmosphere can be mathematically separated. The advantage over the previous surface–atmosphere separation algorithms of Smith et al. (2000a) is that no additional assumptions about surface composition or atmospheric spectral signatures need to be made. This method necessarily requires specific observations and cannot be applied generally to all TES nadir-pointing data, but may be used to provide confirmation and extend the wavelength coverage of previous algorithms. In addition, high-albedo (albedo throughout this paper refers to the Lambert albedo derived from the TES bolometers at 0.3–3.5 μm) region surface spectra can now be derived due to the greater accuracy of this technique.

B. TES instrument description

The TES instrument is a Fourier transform Michelson interferometer that covers the wavelength range from 1700 to 200 cm^{-1} ($\sim$6 to 50 μm) at 10 or 5 cm^{-1} sampling (Christensen et al., 1992). The instrument also contains bore-sighted thermal (5–100 μm) and visible/near infrared (0.3–3.5 μm) bolometers. The focal planes in each wavelength consist of three cross-track and two along track detectors with an instantaneous field of view of $\sim$8.5 mrad. The TES instrument uses a pointing mirror that allows limited targeting capability, limb observations, image motion compensation (IMC), emission phase function measurements, and periodic calibration by observing space and an internal reference surface. The final 2-h, $\sim$380-km altitude mapping orbit provides a surface sampling of $3 \times \sim 8$ km. The elongated pixel dimension is due to the final mapping orbit of MGS, which began its orbit at 2 AM local time rather than the intended 2 PM because of damage to the solar panel that required lower aerobraking rates. Spacecraft direction relative to the surface is reversed and IMC does not produce adequate results when stepping the mirror in the direction opposite that originally intended. As a result, spatial sampling is smeared in the along-track direction. For a complete description of the instrument as built and instrument operations see Christensen et al. (2001a).

A linear response function for each of the six detectors is derived periodically from observations of space and an internal reference surface of known emissivity and temperature. Three scans each of space and the reference surface are taken and averaged for each detector. The linear response function allows for a simple conversion from raw spectra into calibrated radiance. For a complete description of radiometric calibration see Christensen et al. (2001a).

II. Method

A. Observations

The data used for this study consists of two types of TES multiple emission angle observations (which are referred to here as emission phase functions (EPFs)) of the Martian surface. Standard observations view a point on the Martian surface at seven or nine different emission angles at latitudes between 75°S and 75°N and a local time of $\sim$1400 h. A second type are dense observations, which measure a surface at 49 different emission angles. Most of the EPF observations are made of warm surfaces, ensuring a high signal-to-noise ratio and good contrast between the warm surface and relatively cold atmosphere. Several thousand standard EPF observations have been collected to date by the TES instrument at a rate of 1 per orbit (12/day). Dense EPFs are collected less often; several hundred have been collected to date from a variety of locations between 75°S and 75°N.

Each standard EPF observation collects a total of 270 spectra and each dense EPF collects over 1000 spectra within a time period of several minutes. Emission angles were limited to $<65°$ for this study to provide a maximum factor of $\sim$2 in atmospheric path length for each EPF sequence. In addition, spectra of similar emission angles were averaged (with forward- and aft-viewing emission angles averaged separately) to reduce the computation time required for the nonlinear least-squares algorithm. In this manner, each EPF sequence is reduced to a set of 3–20 spectra (at 2–10 emission angles), each of which is an average of 18–30 individual TES spectra.

Optimally, these observations would focus on a single point on the surface to ensure a constant composition and surface temperature. In reality, a single EPF sequence can cover a significant area (Fig. 1). The TES pointing mirror allows for along-track targeting, but not cross-track targeting, resulting in significant cross-track coverage in equatorial regions due to the rotation of the planet. In addition, significant targeting errors are present in the dense EPF

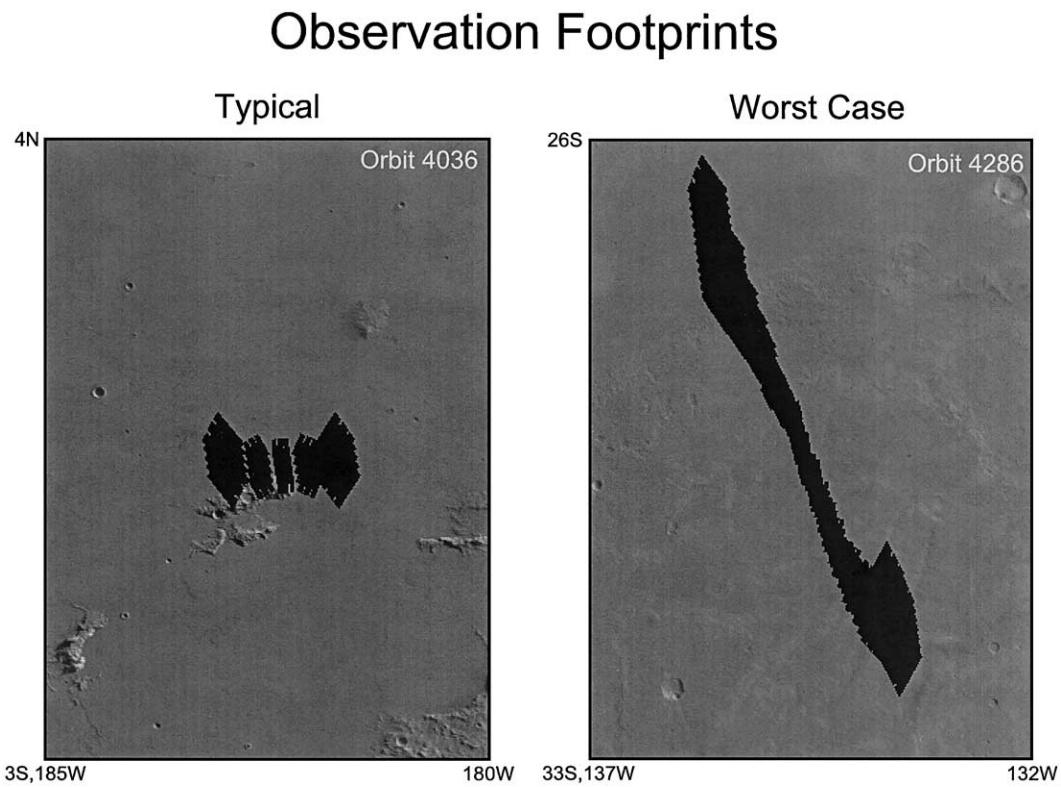

Fig. 1. Spatial coverage of TES EPF observations for a typical-case (left) and a worst-case dense EPF observation (right). Longitudinal spread is a function of latitude and is negligible at the poles and at maximum at the equator because of the rotation of the planet relative to the spacecraft orbit.

observations. This presents difficulties for observing low-albedo regions that are typically variable on the spatial scale of the observations, resulting in significant contributions from surface dust. High-albedo regions are, however, commonly spatially homogeneous and are well suited for these observations. Fig. 2 shows that spatial homogeneity can be present even in low-albedo-region high-emission-angle spectra that were taken farthest apart in both space and time.

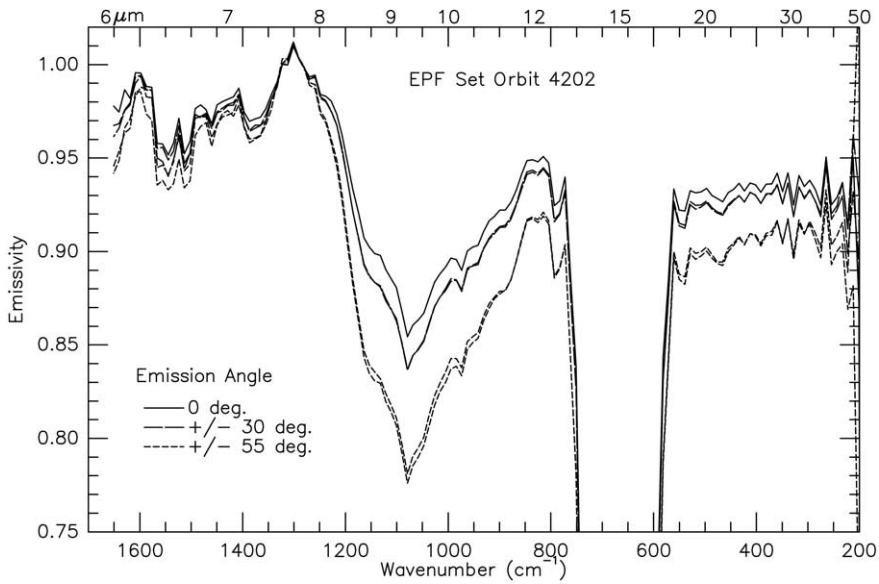

Fig. 2. EPF observation from orbit 4202. All spectra from each of five different TES pointing mirror angles are averaged. Increased absorption from atmospheric dust is apparent from ~300 to 1300 cm^{-1} at higher emission angles. Despite being furthest apart in time in space, the $\pm 55°$ emission angle observations closely match each other.

B. Algorithm description

i. Atmospheric gas removal

Gaseous absorption by CO_2 and H_2O make a significant contribution to the TES spectrum. Water vapor has numerous absorptions that are observable at wavenumbers less than about 450 cm^{-1} and greater than about 1300 cm^{-1}. Carbon dioxide has absorption bands centered near 960, 1060, 1260, and 1365 cm^{-1} that are easily observed (in addition to the extremely strong band centered at 667 cm^{-1} used for temperature retrieval). The amplitudes of gaseous absorption features are often comparable to those of surface mineralogy and so gaseous absorption must be carefully accounted for.

Although the H_2O and minor CO_2 bands are optically thin when convolved to the 6.25 or 12.5 cm^{-1} spectral resolution as observed by TES, many of the individual lines that make up the band are saturated. These lines are very narrow and relatively widely spaced so that when convolved to TES resolution the absorption appears optically thin. Because the individual lines are saturated, they are in the "strong line" regime where observed absorption is proportional to the square root of air mass (or $(1/\cos(\mu))^{1/2}$, where μ is the emission angle). The spectral features caused by H_2O and CO_2 will not separate from those of the surface in the same way that those of dust and water ice will and must be removed and scaled separately.

The absorptions of CO_2 and H_2O are computed using the correlated-*k* method (e.g., Goody et al., 1989). Correlated-*k* coefficients for an array of different temperatures and pressures are computed using a line-by-line computation of CO_2 and H_2O transmittance. Line parameters are obtained from the GEISA-97 database (Hudson et al., 1992). An approximate correction is made to the linewidths to account for CO_2-broadening of water vapor (Smith, 2002).

The contributions from H_2O and CO_2 are computed and removed from each spectrum in the EPF sequence before the application of the main surface–atmosphere separation algorithm that separates the contributions of dust and water-ice clouds from that of the surface. Because the abundance of CO_2 is well known, the radiative contribution of the CO_2 absorptions (as modified by atmospheric dust opacity retrieved from the nadir observation) is directly calculated using the retrieved temperature profile from the nadir observation (Conrath et al., 2000) and removed. Water vapor abundance is variable and unknown, so its contribution is calculated in a manner similar to that of Smith (2002). An index is computed from the low-wavenumber water vapor rotational lines and the synthetic water vapor spectrum is then scaled accordingly throughout the TES wavelength range to determine its radiative contribution. This method has been demonstrated to be robust because the narrow water vapor absorptions are not greatly modified by the much broader surface and aerosol absorptions (Smith, 2002). As a result, water vapor may be accurately isolated by simple continuum removal between local maxima.

ii. Iterative radiative transfer solution

The observed Martian radiance measured by TES can be described by the following equation:

$$I_{\text{obs}}(\nu) = \varepsilon(\nu)\, B[T_{\text{surf}}, \nu]\, e^{-\tau_0(\nu)/\mu} + \int_0^{\tau_0} (B[T(p), \nu]\, e^{-\tau(\nu,p)/\mu}\, d\tau). \quad (1)$$

In this equation, $I_{\text{obs}}(\nu)$ is the measured radiation; $\varepsilon(\nu)$ is the surface emissivity; $B[T_{\text{surf}}, \nu]$ is the blackbody radiance as a function of surface temperature, T_{surf}; $\tau(\nu, p)$ is the normal opacity profile as a function of wavenumber and pressure; and μ is the cosine of the emission angle. The integral is taken through the atmosphere from the opacity at the spacecraft ($\tau = 0$) to the surface ($\tau = \tau_0$); $T(p)$ is the atmospheric temperature profile. The first term accounts for the absorption of surface radiation by the atmosphere; the second (integral) term accounts for radiation emitted by the atmosphere and suspended aerosols. Solar and thermal radiation reflected from the surface as well as secondary scattering are neglected in this equation, and surface radiation is considered to be diffuse. In addition, this analysis assumes that the dust is well mixed with the CO_2 gas and not stratified at any level in the atmosphere. The effect of these assumptions will be discussed below.

A simple nonlinear least-squares fitting algorithm was developed to solve for both surface radiance and atmospheric opacity for the entire TES spectral range. Each spectral band is treated independently and the surface radiance and atmospheric opacity are adjusted iteratively until differences between measured and modeled TES radiances are minimized. The algorithm is stable and a variety of initial guess surface emissivities and atmospheric opacities converged on the same result for a variety of TES observation conditions.

Multiple emission angle observations do not provide any distinction between surface emissivity and surface temperature. For example, the surface-emitted radiance may be the same where surface emissivity is relatively higher and surface temperature is relatively lower than another surface. As a result, the algorithm solves for surface radiance, which is separated into kinetic temperature and emissivity by dividing out a Planck curve of the highest brightness temperature within any 50 cm^{-1} window of the surface spectrum. This is identical to the method used for laboratory emissivity measurements (Christensen and Harrison 1993; Ruff et al., 1997).

C. Uncertainties

Christensen et al. (2000a) and Christensen et al. (2001) have characterized the radiometric precision and accuracy of the TES instrument. The error for the average of six detectors is $\sim 1.2 \times 10^{-8}$ W cm^{-2} str^{-1} cm^{-1} between 300 and 1400 cm^{-1}. For a surface temperature of 280 K, this

translates to an emissivity error of <0.0013 from 300 to 1100 cm^{-1}, increasing to 0.0035 at 1400 cm^{-1}. These errors are reduced somewhat for this study because several dozen to hundreds of spectra are used for each observation, though the random errors from reference calibration observations are not reduced.

An additional systematic error is introduced as a result of a slight optical misalignment in the TES instrument (Christensen et al., 2001). This results in a background radiance error that is dependent on the pointing angle of the TES mirror. This background radiance is generally smooth as a function of radiance with amplitudes of $\leq 7 \times 10^{-8}$ W cm^{-2} str^{-1} cm^{-1} for the pointing angles used in this study. These errors are generally opposite in sign for pointing angle pairs (e.g., $-30°$ and 30°), however. This minimizes the effect because the observations used for this study contain symmetrical sets of pointing angles. In addition, the smooth nature of the background radiance error prohibits the introduction of false mineralogical-type features.

In addition to instrument limitations, a second source of error lies in the assumptions of the atmospheric model. This includes an atmosphere with well-mixed atmospheric constituents as well as nonscattering aerosols. These assumptions are similar to those discussed in Smith et al. (2000b), who concluded that dust aerosols are well mixed most of the time and that a nonscattering model causes a 10–25% underestimate of opacity. The results of Smith et al. (2000b), as well as the results presented here, demonstrate that surface emissivities are constant over widely varying atmospheric conditions and a factor of three variation in dust opacity. There are, however, many cases where atmospheric water ice is not well mixed (Pearl et al., 2001) and observations with significant quantities of water ice must be avoided for accurate separations.

An additional source of error may be found in the atmospheric temperature retrievals and removal of atmospheric gasses. These were estimated to be <2K by Conrath et al. (2000). Incorrect removal of minor CO_2 and water vapor features may cause errors in several wavelength regions. These features are narrow and distinctive, however, and an incorrect removal of them is apparent in the retrieved spectral shapes.

The model used here also assumes that the surface radiance emitted is constant over all angles. While this may be a good assumption for surfaces with particle sizes larger than the wavelength of observation, it is not true for fine-grained surfaces (Jakosky et al., 1990). There are significant surface phase function effects in the TES data present over many high-albedo regions (Bandfield et al., manuscript in preparation). These effects are not present for coarse-particulate surfaces obtained in the field (Jakosky et al., 1990) or the laboratory. As a result, surface features may be mapped into the atmospheric opacity spectrum and surface emissivity absorptions are shallower. Where these effects are present, atmospheric opacity spectra are not retained. However, though spectral contrast may be significantly reduced, the spectral shape of high-albedo surfaces is not affected by phase function errors.

The most significant potential source of error is the variation of surface temperature and composition observed within each EPF observation. As discussed above, there is a significant spread in observation location for each angle of a single observation sequence. This commonly results in a surface temperature range of 3–5 K and significant differences in surface radiance measured at each emission angle. Because these differences are not dependent on emission angle, they are essentially averaged out as a result of the least-squares fitting. The resulting error is similar to that of converting an anisothermal radiance spectrum to emissivity using a Planck curve of a single temperature.

To better understand the effect of these uncertainties on the retrieval, synthetic multiple emission angle radiance spectra were constructed with the known or estimated uncertainties added. These uncertainties include TES random noise derived from space observations, the best estimate of background radiance for each of the five pointing angles used for the simulation, a systematic atmospheric temperature error of $+3$ K, and a variable surface temperature ranging from 275 to 285 K. Synthetic spectral shapes approximating the atmospheric dust and fine particulate basaltic surface and a typical warm-atmospheric temperature profile were used to construct the synthetic spectra. The maximum nadir opacity was 0.4 and the maximum emissivity of the surface was 0.98.

This synthetic observation was then input into the nonlinear least-squares algorithm to retrieve the original surface temperature, surface emissivity, and atmospheric opacity. The results are shown in Figs. 3 and 4. The retrieved surface temperature of 279.2 K is a slight underestimate of the average surface temperature of 280 K. This is because the true maximum surface emissivity of 0.98 is less than the assumption of a maximum emissivity of unity used here. This temperature error imparts an offset and slight slope to the retrieved surface emissivity. The RMS error for the surface emissivity is 0.0126 for 300 to 1650 cm^{-1}. By accounting for the slope and offset by assuming a maximum emissivity of 0.98, the RMS error in the surface emissivity is 0.0026 for 300 to 1300 cm^{-1} and 0.0136 from 1300 to 1650 cm^{-1}. Atmospheric temperature errors do not greatly affect the surface retrieval. A temperature error of $+3$ K at an opacity of 0.4 shallows the retrieved surface emissivity by a maximum of 0.002.

The atmospheric opacity spectral shape is much more sensitive to atmospheric temperature errors. The error in retrieved maximum opacity is ~ 0.01 for each degree of error. This error is an upper limit and will be less in lower dust loading conditions. In the synthetic case presented here; a $+3$-K temperature error results in a maximum opacity of 0.43 versus the true opacity of 0.4. The recovered spectral shape of the atmosphere is accurately recovered with an RMS error (using the correct atmospheric temper-

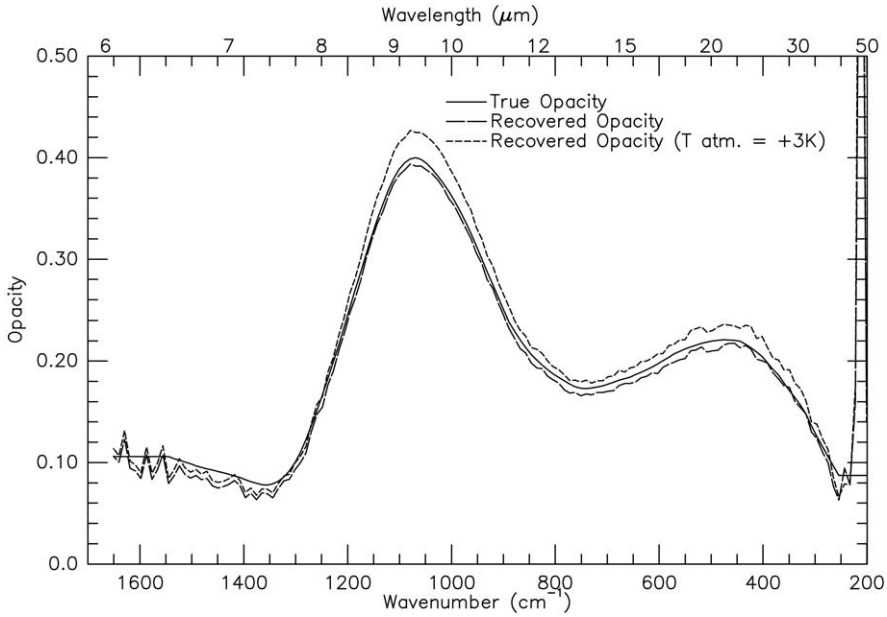

Fig. 3. Example of retrieval of a synthetic atmospheric opacity shape. The original opacity (solid line) is well approximated when the correct atmospheric temperature profile is used (long dash). Opacities are overestimated (short dash) or underestimated with a temperature profile that is above or below the true temperature respectively.

atures) of 0.0064 from 300 to 1300 cm^{-1} and 0.013 from 1300 to 1650 cm^{-1}.

An additional set of synthetic observations was created to test the effects of scattering on the retrieval algorithm. The extinction and single scattering albedo of the atmospheric dust were estimated from both limb and nadir TES data to provide an approximation for the dust properties. Two sets of synthetic radiance spectra were produced for a 280-K surface with a typical warm atmospheric profile at emission angles of 0°, 30°, and 60°. The first set of synthetic spectra was produced using radiative transfer software that computes the observed radiance at a given viewing angle from a surface and an atmosphere containing scattering aerosols. Scattering is treated using the discrete ordinates approximation (e.g. Toon et al., 1977; Goody and Yung, 1989). The second set was produced without the scattering

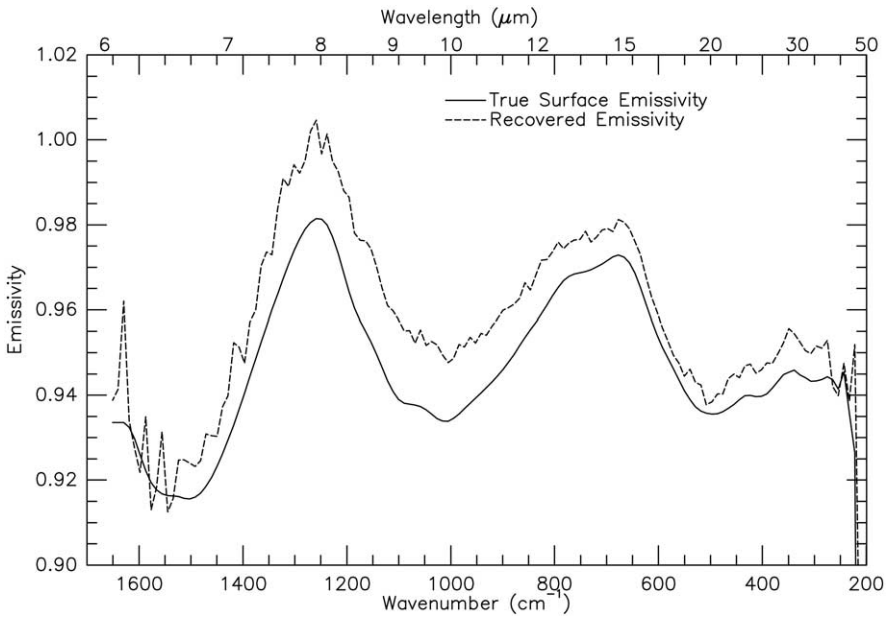

Fig. 4. Example of retrieval of a synthetic surface emissivity shape. Though the original (solid line) and retrieved (dashed line) spectra are offset, the spectral character is accurately recovered. The offset is due to the requirement that the algorithm assume a maximum emissivity of 1.

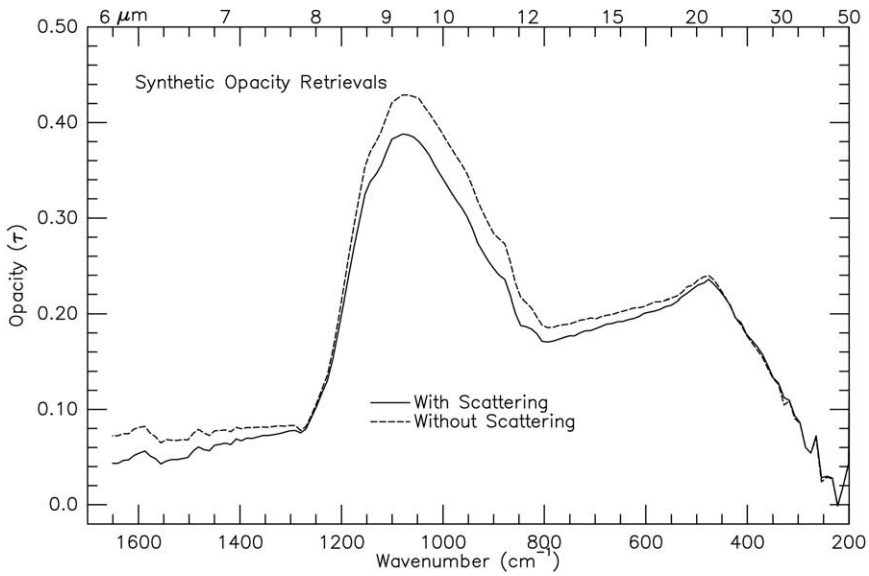

Fig. 5. Effect of scattering on the opacity retrieval. Adding scattering to the synthetic spectral sets causes a 10% decrease in the peak opacity values (solid line) over the retrievals using synthetic spectra constructed without scattering (dashed line).

term. The difference in the opacity retrievals is displayed in Fig. 5. Peak retrieved opacity values are underestimated by 10% in the case where scattering is included in the synthetic EPF set. This is at the lower end of the scattering uncertainty estimate of Smith et al. (2000b) and opacity retrievals presented here are approximately 10% lower than their true values.

III. Results

Surface emissivity and atmospheric opacity spectra were recovered from all 10 cm^{-1} sampling TES EPF observations to MGS orbit 5317 (L_s 104–352). The orbit range was restricted due to an instrument anomaly that grew progressively worse past this period. This anomaly causes a sporadic minor feature to appear in spectral data near 1000 cm^{-1}. The cause of this anomaly is unclear at this time, though it is similar to other features that are correlated with spacecraft vibrations.

This dataset was reduced considerably based on several criteria. Observations with significant water ice ($\tau_{ice} \approx 0.05$) were excluded as it is commonly not well mixed in the atmosphere (Pearl et al., 2001) and does not closely fulfill the assumptions required for an accurate separation. Dust opacities near 1080 cm^{-1} were limited to <0.5 to minimize the effects of scattering. Surface temperatures were limited to those greater than 275 K to ensure a high signal to noise ratio. In addition, retrievals with high sample-to-sample noise levels were also excluded though the surface temperatures are >275 K.

The locations of the limited set of EPF observations are shown in Fig. 6. While longitudinal coverage is widespread, observations are limited to latitudes of 15°N to 60°S as a result of both the requirement for warm surface temperatures and the seasonal timing of EPF observation targeting. Several geographical gaps persist within this latitude range, including Hellas and Argyre basins because of high dust opacities and much of the Tharsis rise as a result of persistent atmospheric water ice.

The resulting spectral shapes were separated into three categories; moderate- to high-albedo surfaces (Lambert albedo >0.18), low-albedo surfaces (Lambert albedo <0.18), and atmospheric dust. The high-albedo surface spectral shapes all contain little or no absorption near 400 and 1000 cm^{-1} with prominent absorptions near 800 and >1300 cm^{-1}. This shape is similar to that inferred by Ruff and Christensen (in press) through ratioing TES spectra. Low-albedo surface spectral shapes contain little or no absorption at wavenumbers >1300 cm^{-1} and prominent absorptions near 300–500 and 900–1100 cm^{-1}. Atmospheric opacity spectral shapes were limited to observations with no detectable water ice opacity (based on the deviation of the dust shape in the region 11–12 μm as well as based on comparison with previously derived dust spectral shapes) as well as no significant surface phase function effects. These exclusion criteria result in 24 low-albedo and 65 high-albedo surface emissivity spectra as well as 42 atmospheric dust opacity spectra.

Each average spectral shape is shown in Fig. 7. Each individual spectrum was normalized to the average spectrum and the standard deviation for each spectral shape was calculated. Standard deviations are <0.005 for both surface spectral shapes and <0.01 for the atmospheric dust opacity spectrum between 400 and 1300 cm^{-1}. Deviations are higher at both the low- and high-wavenumber ends of the

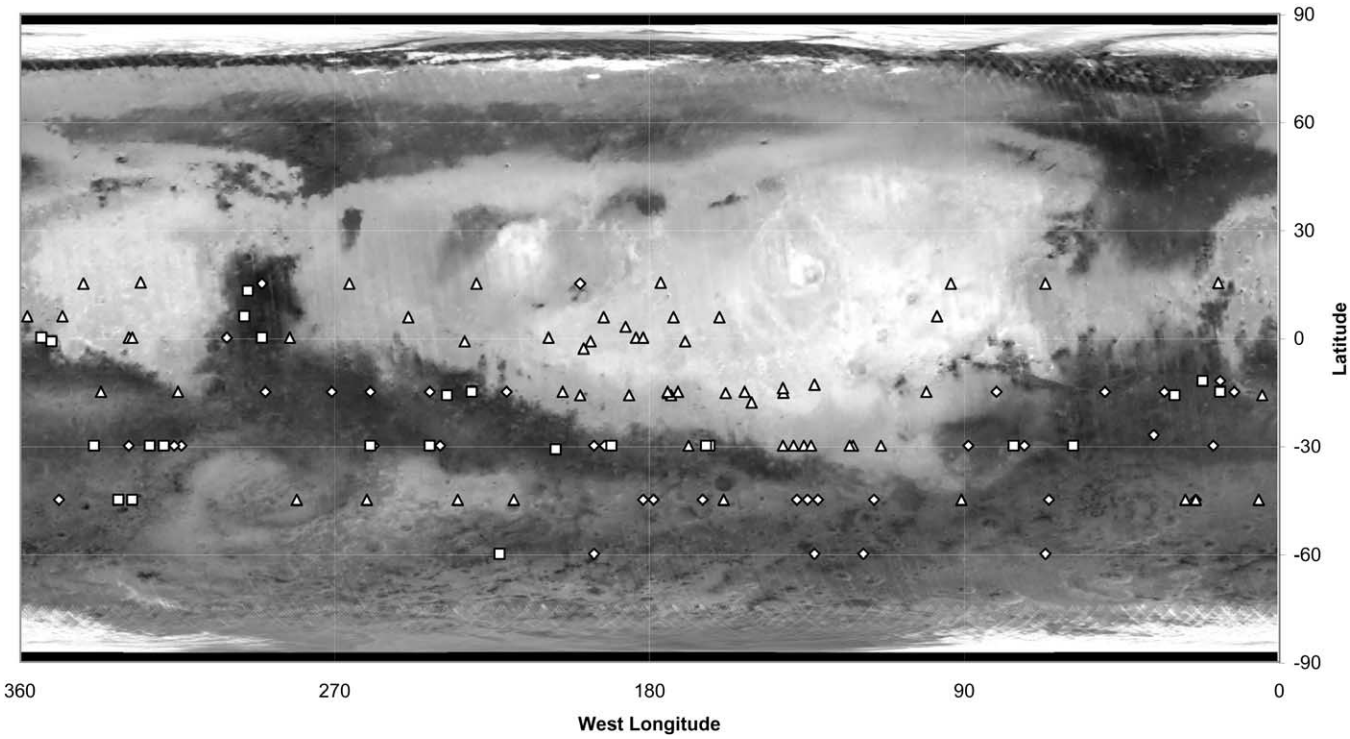

Fig. 6. Locations of EPF observation sequences used for this study. Triangles are moderate- to high-albedo surfaces, squares are low-albedo surfaces, and diamonds are atmospheric dust retrievals.

TES spectral range due to lower signal to noise and uncertainty due to water vapor removal.

IV. Discussion

A. Dust opacities and surface temperatures

i. Comparison with previous shapes

The atmospheric dust opacity spectral shape is similar to those isolated by Bandfield et al. (2000a) and Smith et al. (2000a) (Fig. 8). Several important differences exist, however. Both the emissivity dust shape of Bandfield et al. (2000a) and the dust opacity shape of Smith et al. (2000a) were derived from nadir observations and a wavelength of atmospheric transparency was assumed, which adds an offset error to both of the previous shapes. Minor CO_2 isotope and "hot band" absorptions were not removed from the emissivity shape and were only partially accounted for in the previously derived opacity shape. Water vapor is also not removed from either of the two previous shapes. These disparities are apparent in the differences between the EPF derived opacity spectrum and the normalized, previously derived spectral shapes (Fig. 8).

ii. Compositional and particle size implications

Bandfield et al. (2000a) noted the stability of the atmospheric dust spectral shape over widely varying dust loadings and seasons. The dust opacity spectra presented here reinforce this result. The recovered atmospheric opacity spectra cover a factor of 3 difference in dust loadings as well as the 2000 dust storm season (L_s 196–312). No significant differences are present between dust opacity spectral shapes from any season or dust loading (Fig. 9). This demonstrates that compositional variation and changes in the particle size distribution (for particles with radii on the order of $\sim$1–10 μm) are not significant in the atmospheric dust over the course of the Martian dust storm season. The constant nature of the thermal infrared spectral response of the Martian airborne dust has been demonstrated for the dust storm seasons of 1971–1972 (Toon et al., 1977), 1997–1998 (Bandfield et al., 2000a), and 2000. This study does not include the 2001 dust storm season, however, which achieved 9-μm dust opacities of >2 (Smith et al., 2002). There is evidence for variations in particle size during this season (M. Wolff, personal communication) and more sophisticated retrieval algorithms will be useful for the analysis of the 2001 dust storm data.

iii. Comparison with TES database opacity and surface temperature retrievals

Surface temperatures may be derived more precisely using multiple emission angle observations than with the standard TES nadir observations. The method of surface kinetic temperature determination used in the nominal TES processing assumes that the atmosphere is transparent at the

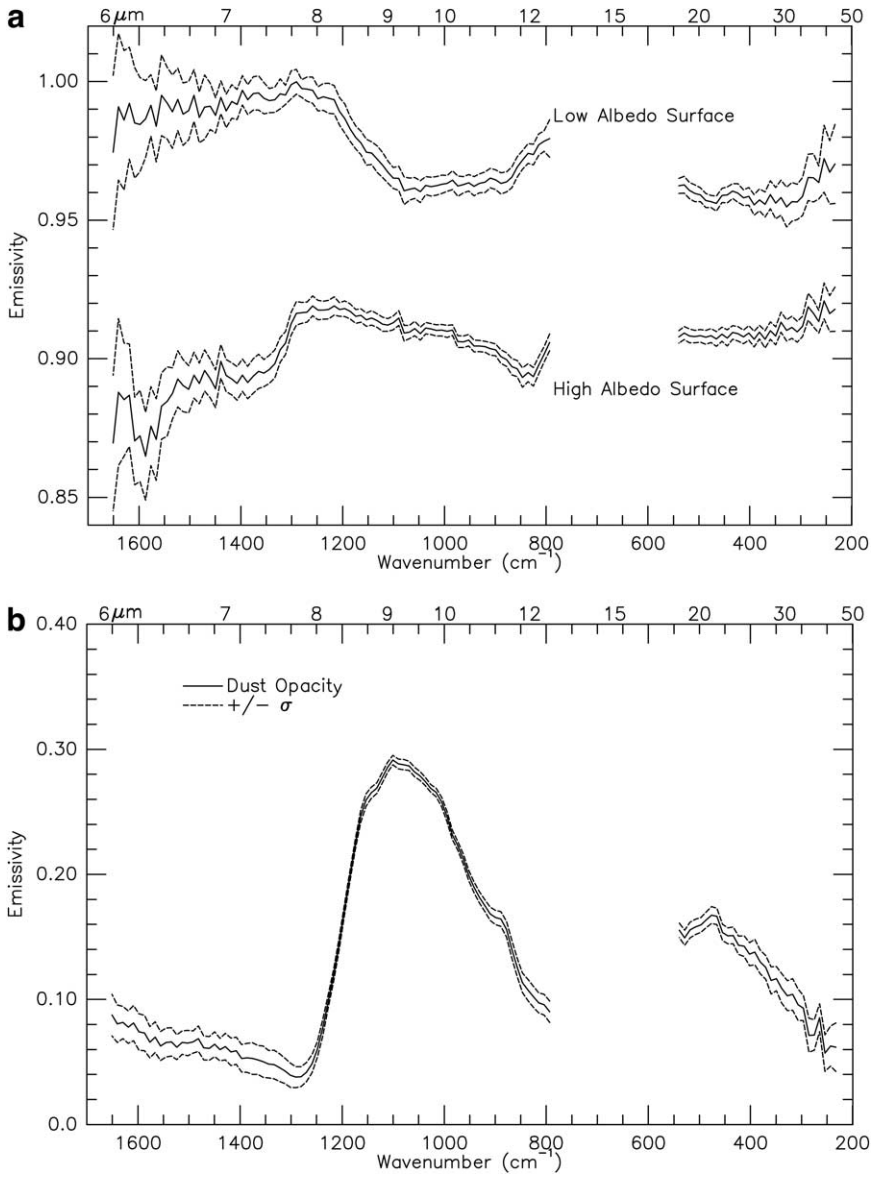

Fig. 7. Retrieved TES surface and atmosphere spectral shapes and standard deviations. (a) Average low-albedo and moderate- to high-albedo surface spectral shapes. The high-albedo surface spectrum is offset by 0.08. (b) Average atmospheric dust spectral shape. Dotted lines represent $\pm\sigma$ errors for each spectral type.

wavelength of the highest brightness temperature (typically near 1300 cm^{-1}). This assumption is unnecessary for surface temperatures derived using the TES EPF observations. The differences between surface temperatures derived from the nadir only observations and the TES EPF observations are shown in Fig. 10. There is a general correlation between opacity and the magnitude of the error. For the relatively warm surfaces with relatively cold atmospheric temperatures, nadir surface kinetic temperatures are underestimated by ~1–3 K for 9-μm dust opacities of ~0.15–0.3 and ~2–4 K for opacities of ~0.3–0.5. This underestimate is greatly affected by the temperature difference between the atmosphere and the surface and, as a result of the lower temperature contrast, is not as significant for nighttime observations. Daytime surface temperatures may still be underestimated in this study by $<\sim$1K, however. This is due to the assumption of a surface emissivity of 1 at the wavelength of maximum brightness temperature for the temperature retrieval.

The lack of an atmospheric transparency wavelength also affects derived nadir dust opacity values. The TES nadir and EPF-derived 9-μm dust opacity values are compared in Fig. 11. As expected, the nadir dust opacities derived using the method of Smith et al. (2000a, 2000b) underestimate the atmospheric dust loading by typically 0.05–0.12.

B. Low-albedo surfaces

Low-albedo surfaces display significant absorptions near 300–500 and 900–1100 cm^{-1}, consistent with coarse-

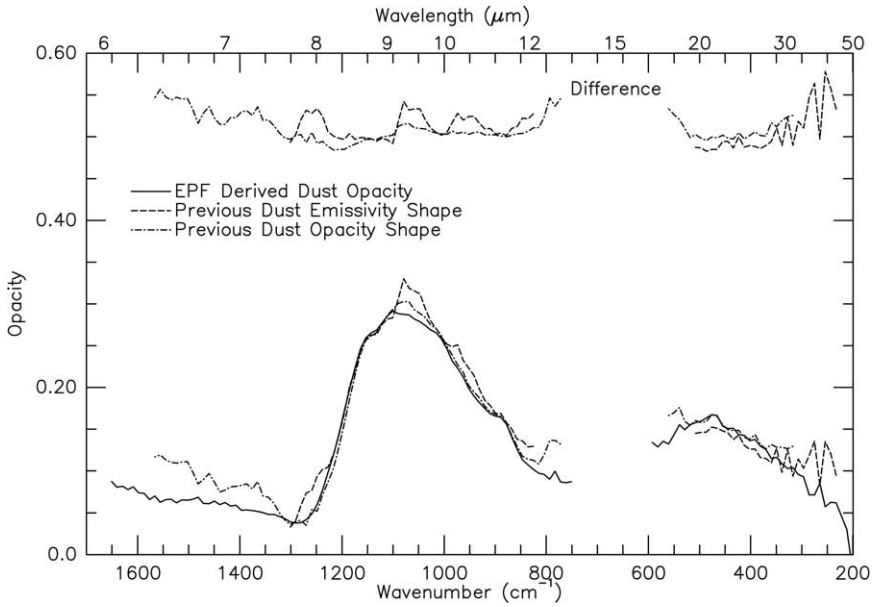

Fig. 8. Comparison of atmospheric dust spectral shape (solid line) with normalized dust shapes used in Bandfield et al. (2000b) (dashed line) and Smith et al. (2000a) (dot–dash). The difference spectra are offset by 0.5.

grained silicates. This spectral shape compares well, to first order, with previously recovered low-albedo surface spectral shapes and confirms a basic to intermediate volcanic composition (Bandfield et al., 2000b; Christensen et al., 2000a; Bandfield 2002).

Compared with high-albedo surfaces, the low-albedo surface spectra have relatively high standard deviations because of significant variations in surface composition. Most low-albedo regions on Mars may be characterized by some combination of two spectral shapes representing basaltic and andesitic mineralogies (Bandfield et al., 2000b; Bandfield 2002). In the equatorial and southern hemisphere regions covered by the observations used for this study, low-albedo surfaces are typically dominated by a basaltic composition though variable contributions of the other surface type are also commonly present.

The large footprint of each multiple emission angle sequence makes it difficult to avoid surfaces with significant contributions of dust cover. The relative contribution of dust cover also contributes significantly to the retrieved surface

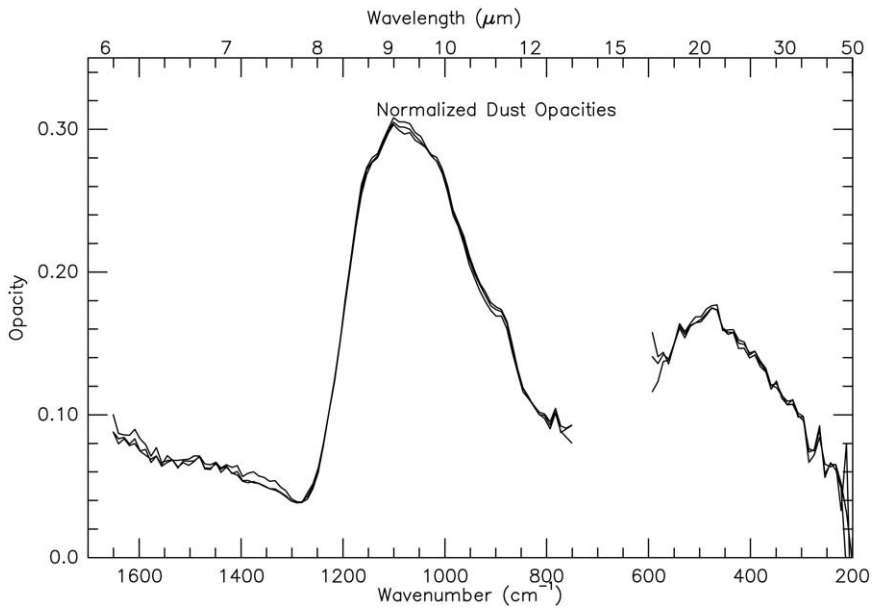

Fig. 9. Normalized dust opacity shape from periods of low, moderate, and high-dust opacity. The spectral shape displays no significant change despite a factor of 3 difference in atmospheric dust loading and a variety of seasonal observations.

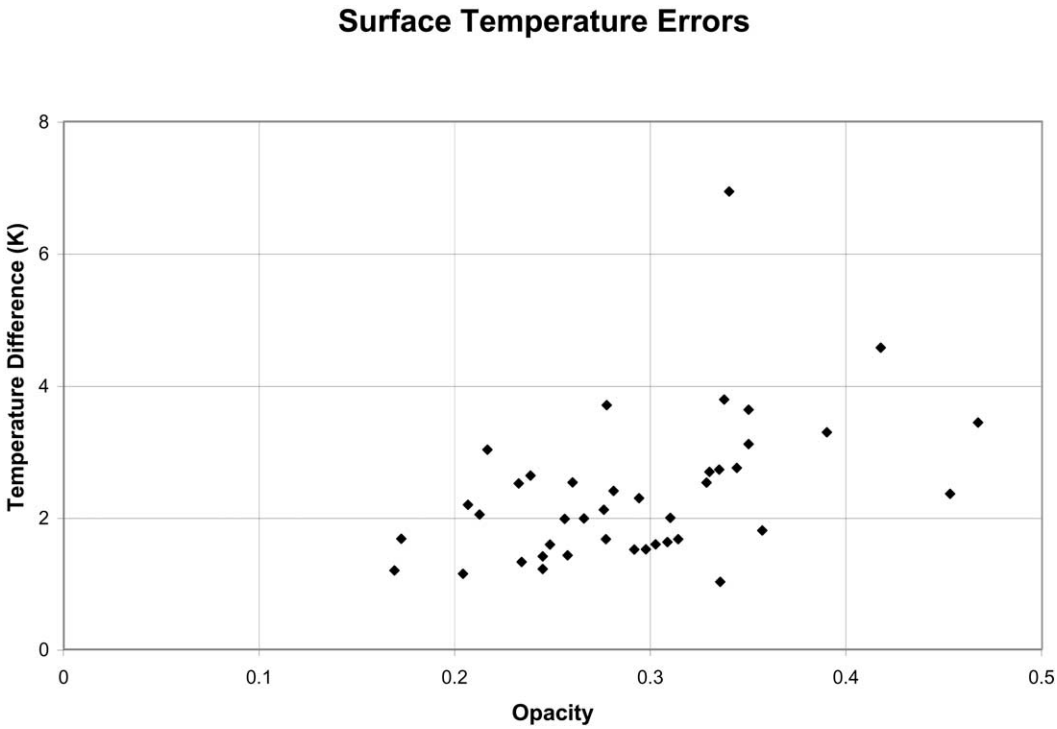

Fig. 10. Underestimate of surface temperature using nadir-only observations versus dust opacity. Though there is significant scatter that is most likely due to the greater surface area of measurement of the EPF observation derived temperatures, there is a trend to increasing error with increasing dust opacity.

emissivity. The average low-albedo surface spectrum may be closely modeled using a linear combination of the two low-albedo surface spectral types from Bandfield et al. (2000b) and the average high-albedo surface spectrum retrieved in this work (Fig. 12). The relative weightings are 36% basalt, 12% andesite, and 52% dust. RMS error between the retrieved spectrum and the linear least-squares fit is 0.0014. These relative weightings are consistent with the

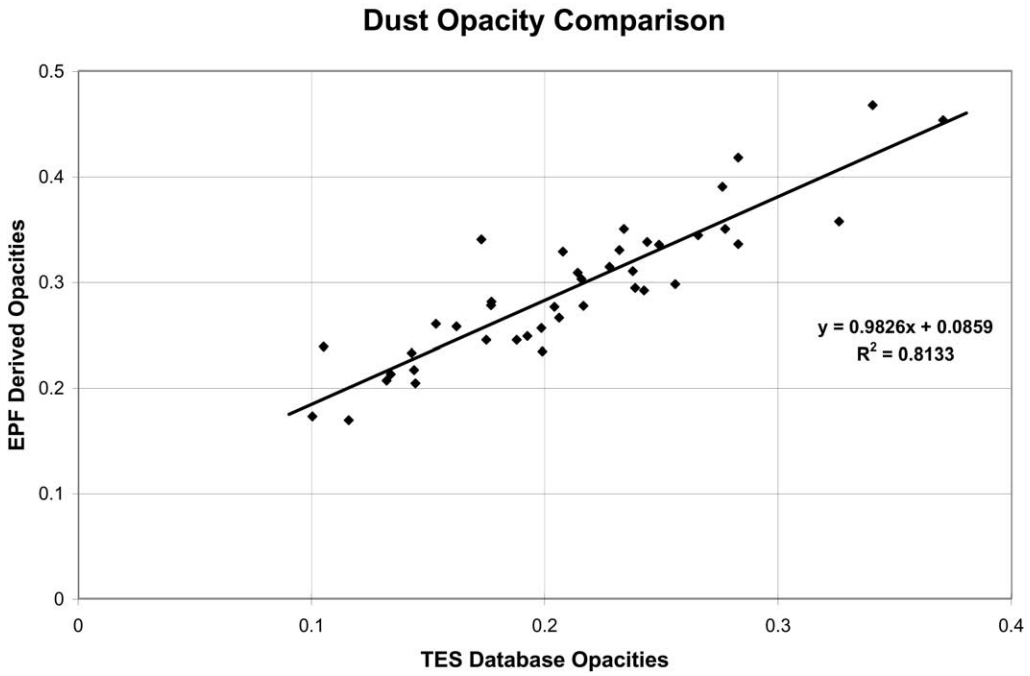

Fig. 11. EPF observation dust opacities versus nadir-only observation opacities. The correlation between the two measurements is nearly perfect with a constant offset of about 0.08. It is unclear why this offset is present.

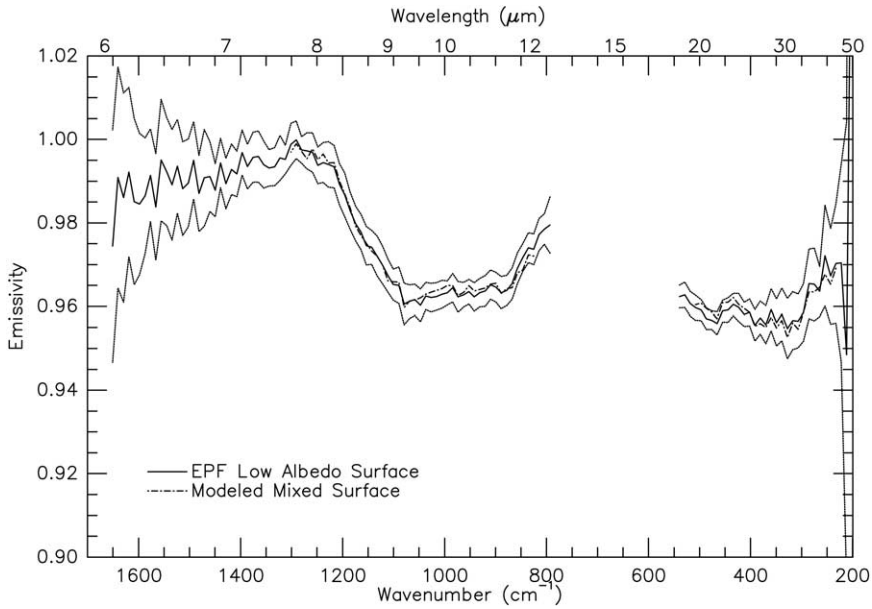

Fig. 12. EPF-derived low-albedo surface spectrum (solid line) compared with a mixed surface of 36% basalt and 12% andesite from Bandfield et al. (2000b) and 52% surface dust from this study (dot–dash). The wavelength range of the fit is limited due to the coverage of the basalt and andesite spectral shapes. The $\pm\sigma$ error on the EPF derived low-albedo surface spectrum is shown by the dotted lines.

concentrations of each surface type by Bandfield et al. (2000b) within the regions covered by this study. This result adds confidence to previous atmospheric correction results, but the low spatial resolution and the large dust contribution prevent more precise compositional determination.

The extended wavelength coverage relative to previous studies allows for some refinement of previous results. The 1300–1650 cm^{-1} portion of the low-albedo surface spectrum is featureless and does not contain significant absorptions ($>$0.985 emissivity). Much of the small amount of absorption present in this region can also be attributed to the surface dust contribution discussed above. The lack of dominant particle size effects is consistent with both the spectral contrast present and thermal inertia values indicative of a surface composed primarily of sand-sized particulates (Kieffer et al., 1977; Mellon et al., 2000; Bandfield et al., 2000b; Christensen et al., 2000a, 2000b).

It is also possible to directly restrict the carbonate abundance based on a visual inspection because of the smooth continuum and the presence of a strong carbonate absorption in this spectral region. Though the noise is significant within this spectral region, the spectrum does not deviate from the continuum systematically and it is possible to place a limit on the signal strength of carbonate present (Fig. 13). It is possible to limit the abundance by visual inspection to less than 5% if the carbonate has a similar texture and particle size as the rest of the low-albedo surface. This abundance limit will be about $\sim$3% if the carbonates are present in the form of clasts or bedrock, which have higher spectral contrast (Ruff 1998). Christensen et al. (2000b) discusses the relation between particle size and abundance as applied to hematite in detail and the relation is similar with carbonates and other materials.

C. High-albedo surface

i. Physical properties

The high-albedo surface spectral character has not been derived before this study due to the limitations of the previously developed atmospheric correction techniques (Smith et al., 2000a; Bandfield, 2002). As will be discussed below, high-albedo surfaces display distinctive thermal infrared signatures characteristic of fine particulate silicate materials. There are no apparent spectral differences present between any of the locations used for this analysis, though the intensity of the features may change considerably. The dominance of transparency features in the spectrum over the restrahlen bands indicates that the spectral signature is dominated by particle sizes of $<\sim$40 μm (Salisbury and Walter 1989; Ramsey and Christensen 1998). As is the case with the lunar regolith, larger particles may be present as agglomerates of these fine particulates and still behave spectrally similarly to the finer size fraction (Salisbury et al., 1997).

The locations of the recovered high-albedo surface spectra are within surface units that have a Lambertian albedo of $\sim$0.18–0.35 and thermal inertias of $\sim$50–550 J m^{-2} K^{-1} (Mellon et al., 2000). This includes not only the high-albedo, low-thermal-inertia surfaces, which are presumably mantled by fine dust, but also surfaces with both moderate to high albedo and thermal inertia. Regions such as Oxia Palus are characteristic of a distinct surface that has mod-

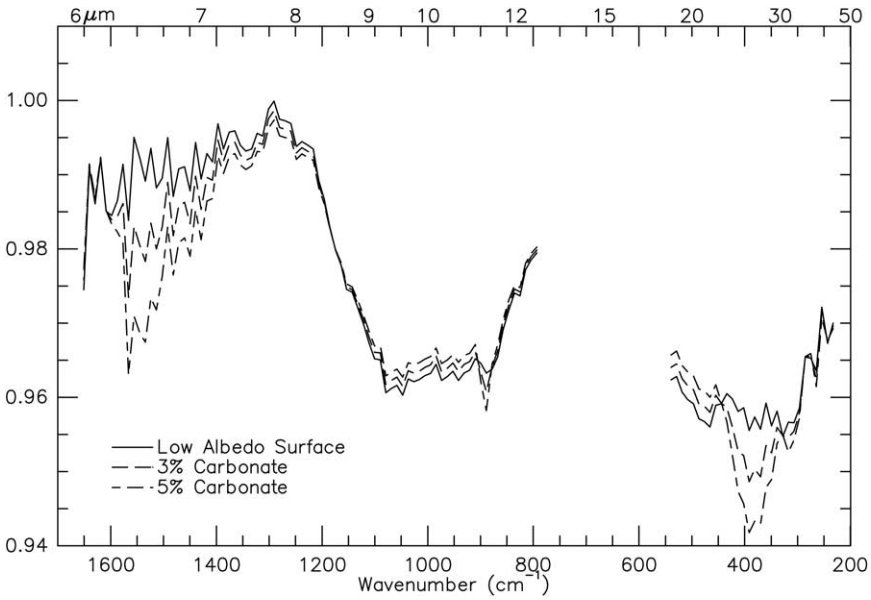

Fig. 13. EPF-derived low-albedo surface compared with synthetic surfaces with 3% and 5% carbonate added. The carbonate sample is a solid dolomite sample (ASU spectral library sample 142) and has the equivalent spectral contrast of ~5% and 9%, respectively, if the sample was a coarse particulate similar to Martian low-albedo surfaces. The lack of any significant spectral absorptions in the wavenumber range 1300–1650 cm^{-1} precludes any significant carbonate abundance in low-albedo regions.

erate albedo and thermal inertia values that has been interpreted to be indurated soil material (Arvidson et al., 1989; Mellon et al., 2000). The nature of the surface spectra is similar to those of higher albedo, dust-mantled surfaces. This indicates that some significant portion of the surface must be loose fine particulate material and is not consistent with an indurated surface. A possible explanation is that both of these surfaces are present within these regions and mix in a checkerboard fashion from millimeter to kilometer scales. This can be observed at both the Viking and Pathfinder landing sites where crusty, indurated material can be seen adjacent to dust mantled surfaces. The indurated surfaces display little spectral contrast (Ruff et al., 2001) and would not contribute significantly to the derived surface spectra. It is not clear if it is plausible to have a surface heterogeneous on the millimeter to kilometer scale be homogeneous on a regional to global scale, however.

ii. Comparison with library spectra

No material could be found that matches all of the spectral features of the high-albedo surface. Several materials match well between ~800 and 1300 cm^{-1}; however, the structure present does not match well at wavenumbers > 1300 cm^{-1} (Fig. 14). This structure at shorter wavelengths can be greatly modified by small amounts of materials with significant absorption coefficients within the same wavelength range (Salisbury and Walter, 1989) such as carbonates (Bandfield et al., manuscript in preparation). Unfortunately, many of the terrestrial samples do not have data at wavenumbers <750-cm^{-1} because the wavelength limitations of the detector used for hemispherical reflectance measurements. Though systematic fine particulate sample libraries are not available for these wavelengths, the lack of significant features at the long wavelengths in the TES spectrum is consistent with silicate mixtures. A number of studies have used emission or biconical reflectance data that extend out to 400 cm^{-1} (e.g., Roush and Bell, 1995; Bishop et al., 1998; Cooper and Mustard, 1999), but these studies cover a limited variety of materials. The lack of Martian spectral features at these wavelengths, the limited variety of samples collected, and potentially significant differences between biconical and hemispherical reflectance preclude the use of biconical reflectance data for an effective study.

It is possible in some cases, however, to determine compositional information by matching individual spectral features and wavenumber ranges. The spectral range 800–1300 cm^{-1} displays a number of similarities to fine particulate spectra of feldspar rich igneous rocks (Fig. 15). The 800-cm^{-1} transparency feature, which may be attributed to feldspar and related mineralogies, is present both in the Martian spectrum and the rock samples with significant feldspar content. An additional feature useful for the interpretation of fine particulate spectra is the Christiansen frequency, or the wavelength of emissivity maximum (e.g., Conel, 1969, Logan et al., 1973, Salisbury and Walter, 1989). The Christiansen frequency of the Martian spectrum is broad and not well defined and is centered near 1250 cm^{-1}. This frequency is coincident with that of intermediate igneous rocks; however, there is ample compositional evidence (e.g., Toulmin et al., 1977, Bell et al., 2000, Bell, 1996) that Martian high-albedo regions are not composed of

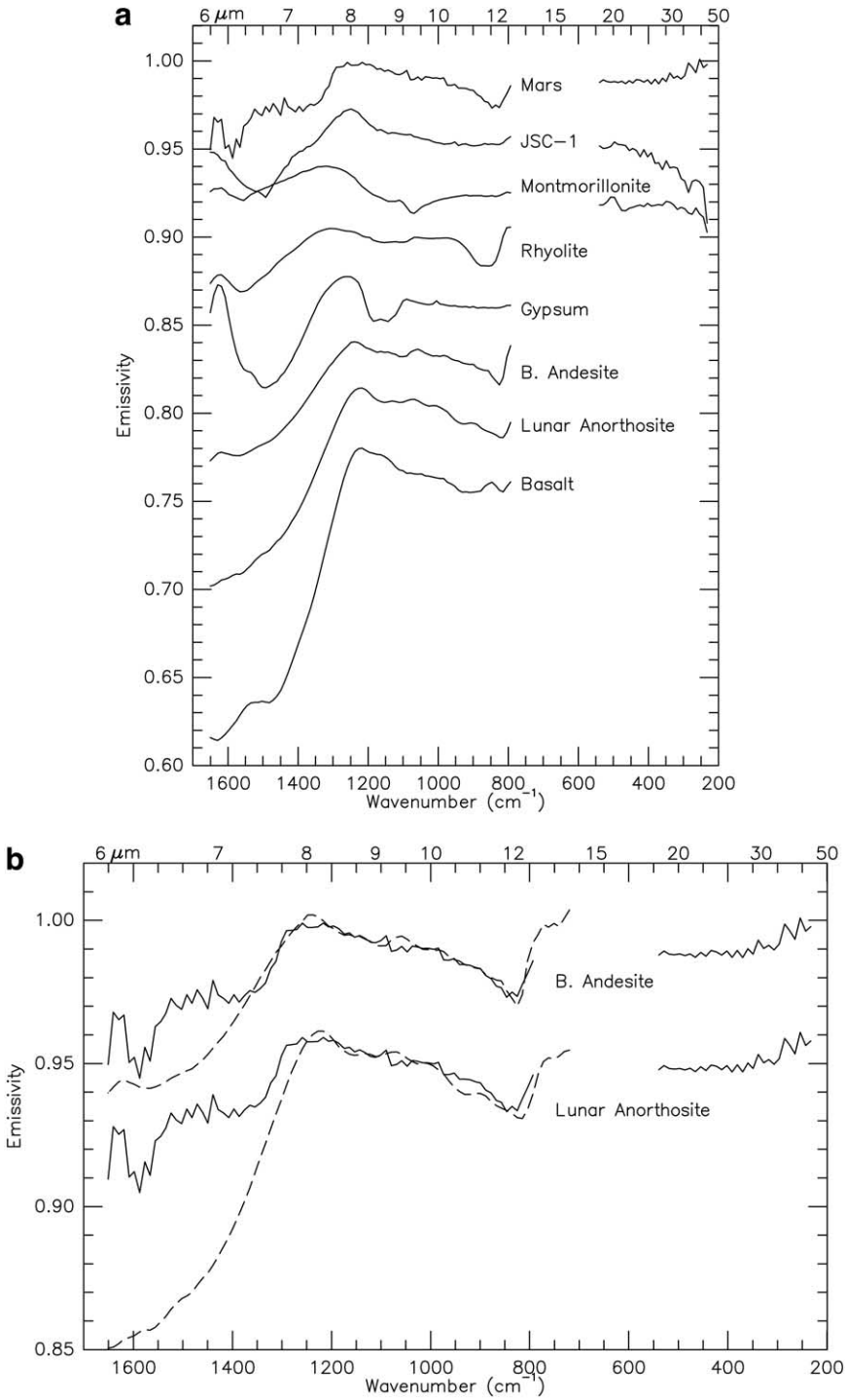

Fig. 14. Comparison of the Martian high-albedo surface spectrum with spectra of several fine particulate materials. (a) Comparison with <63-μm emissivity samples of JSG-1 Martian analog material and montmorillonite powder as well as hemispherical reflectance spectra of <45-μm rhyolite, gypsum, basaltic andesite, lunar anorthosite, and basalt powders (Salisbury and Walter 1989; Salisbury et al., 1997; Grove et al., 1992). All spectra have been offset and normalized to the same relative spectral contrast of the Mars spectrum from 800–1200 cm^{-1}. (b) Comparison with basaltic andesite and lunar anorthosite from Fig. 13a. No contrast enhancement or continuum removal has been applied to any of the spectra. Spectral pairs have been offset by 0.04.

primary igneous material. As a result it is difficult to estimate silica content using the Christiansen frequency.

There is also a dearth of spectral absorption and structure between $\sim$900–1300 cm^{-1}. This is a region of residual restrahlen absorption in fine particulate materials and is commonly present in mafic rocks due to the presence of pyroxene and olivine (Salisbury and Ward, 1989). There is no evidence for the presence of either olivine or pyroxene in

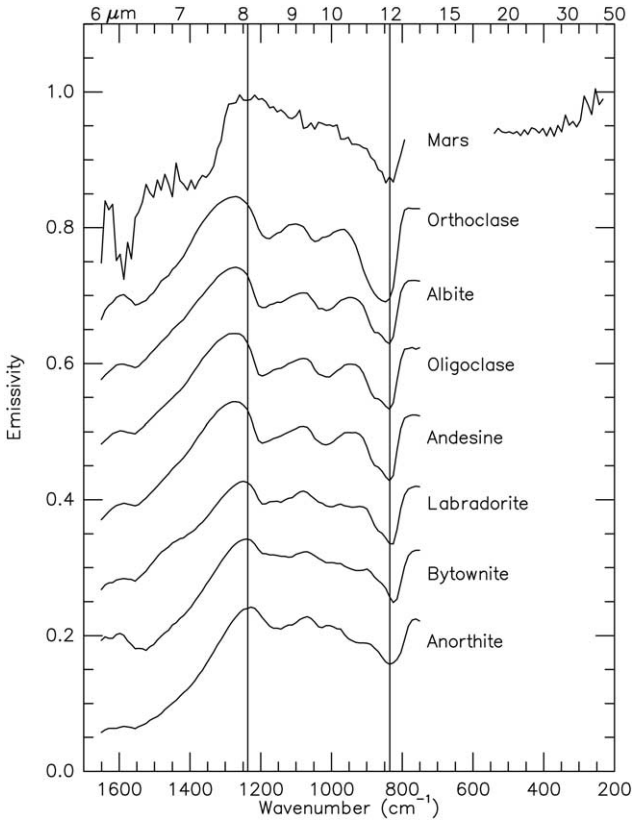

Fig. 15. Comparison of the Martian high-albedo surface spectrum with feldspar materials (Grove et al., 1992). The Mars spectral contrast has been expanded to compare with the individual minerals. Vertical lines represent the center point of the Martian Christiansen frequency and transparency band.

the Martian surface spectrum, though it is difficult to place a limit on the abundance that may be present and not detected. More spectrally inert materials, such as amorphous silicates may be present in significant abundances. There is also little evidence for oxides due to the lack of absorption at wavenumbers $>\sim$600 cm^{-1} where even fine particulate nanophase hematite has significant absorption (Christensen et al., 2000b). Again, it is unclear what abundances of oxides need to be present to be detected, however.

It is difficult to estimate abundances of the feldspar content due to the nonlinear nature of the spectral mixing of the components present in these fine particulates. It is possible, however, to estimate the specific composition based on the position of the spectral features (Fig. 15). Both the Christiansen frequency and the $\sim$800 cm^{-1} transparency feature shift to longer wavelengths with increasing Ca content. Both of these features in the Martian surface spectrum match well with plagioclase in the labradorite to bytownite compositional range.

Though it is difficult to make a compositional match to the high-wavenumber ($>$1300 cm^{-1}) features in the Martian surface spectrum, it is possible to attribute the positive feature near 1600 cm^{-1} to the H–O–H bending fundamental of bound (or possibly adsorbed) water in the surface. This feature is similar to the strong $\sim$3-μm absorption present on the Martian surface (e.g., Pimentel et al., 1974, Bell and Crisp, 1993, Murchie et al., 1993). The exact shape and position of this feature may be variable with different compositions, though it is difficult to ascribe this feature to a specific mineralogy. It is also difficult to determine the abundance of water present, as the strength of this feature is strongly dependent on particle size. A possibility for the source of this spectral feature is a hydroscopic sulfate component, which is widely suspected to be present in the Martian dust (Toulmin et al., 1977, Clark, 1993, Bell et al., 2000). Laboratory studies of sulfate spectra clearly display this feature (Lane and Christensen, 1998, Cooper and Mustard, 2002).

The similarity of this bound water feature to that of atmospheric water vapor may cause some concern about inaccurate water vapor removal. The surface spectral feature is offset to higher wavenumbers relative to the atmospheric features, however, and it is impossible to reproduce the surface water feature through over- or undercorrection of the atmospheric water content.

The Martian surface spectrum indicates the presence of what is consistent with a calcic plagioclase feldspar component with an additional hydrated material. An alternate explanation is the chemically and spectrally similar, but hydrated, zeolite mineral group (Ruff, 2002). There is no evidence for other primary silicate materials including pyroxene and olivine, nor is there evidence for oxide materials in large abundances. Other, more spectrally inert components may be present, including amorphous silicate materials. Laboratory studies are needed in order to better quantify sensitivities and establish the quantities of minerals that need to be present to be detected.

iii. Compositional implications

The mineralogical interpretation presented here is in good agreement with previous visible and near-infrared (VNIR) spectroscopic results. The presence of bound water due to the $\sim$1600 cm^{-1} emission peak agrees well with the 3-μm absorption, indicating that molecular water is present at the surface. The 1600 cm^{-1} feature is not detectable in low-albedo regions due to the coarse particulate nature of those surfaces. Volume scattering is greatly reduced within the TES spectral range and it is a more linear spectral mixing environment. This is not the case at shorter wavelengths, such as 3 μm, and the water absorption is retained for coarse particulate surfaces. The water absorptions at both wavelength regions are not particularly suited for determining mineralogy and the hydrated phase has not been identified.

Neither the results presented here nor previous visible and near infrared spectral results display any signature associated with ferrous (Fe^{2+}) mineralogies for high-albedo regions. The high-albedo surface spectrum displays no residual restrahlen features associated with pyroxene or olivine that are commonly present in fine particulate mafic

compositions (Salisbury and Ward 1989). Other spectroscopic observations in the VNIR display clear evidence of ferric compositions, but no evidence of ferrous absorptions that are clearly present in low-albedo regions (see summary in Bell (1996)).

Previous VNIR spectroscopic studies are not sensitive to feldspar content while the results here are not sensitive to minor amounts of ferric oxides. There is little evidence for major amounts of oxide materials such as hematite, but previous spectroscopic results have detected minor amounts of crystalline hematite (Bell et al., 1990) as well as nanocrystalline iron oxide materials (e.g., Morris et al., 1989). The abundances present are well below what abundances of these materials could be detected with confidence at the thermal infrared wavelengths. Alternately, feldspar is difficult to detect in any quantity in the VNIR wavelength range, but is readily detected in significant abundances in both coarse and fine particulate surfaces in the thermal infrared. The use of a wide variety of wavelengths for spectral studies provides complimentary mineralogical information about the Martian surface.

iv. Comparison with previous chemical and spectral results

Both the Viking X-Ray Fluorescence Spectrometer (XRFS) (Toulmin et al., 1977; Clark et al., 1982) and the Mars Pathfinder Alpha Proton X-Ray Spectrometer (APXS) returned elemental data of the Martian surface (Rieder et al., 1997; Bell et al., 2000). The elemental abundances are similar between Viking and the Pathfinder landing sites (Toulmin et al., 1977, Foley et al., 2001) and it is presumed that if the materials are not the same, they are similar.

Toulmin et al. (1977), Gooding (1992), and Bell et al. (2000), have attempted to recast the elemental abundances in terms of normative mineralogy. These researchers have found it difficult to find a suite of minerals that match the Viking and Pathfinder elemental abundances well. Combinations of materials dominated by phyllosilicate alteration products have most closely matched these abundances. An ambiguity in the studies of Gooding et al. (1992) and Bell et al. (2000) has been whether to cast the A1 content into illite (38–65%), a secondary mineral, or unaltered plagioclase (23–48%) (Bell et al., 2000). The results presented here indicate that at least some plagioclase is likely to be present in the Martian soil and that the normative mineralogies are more accurate if it is included.

Other normative minerals included large abundances of smectite clays (20–64%) and lesser amounts of sulfates (8–16%) and oxides (1–6%). None of these materials are detected in the Martian surface spectrum, but the sulfates and oxides would likely not be detected in these abundances for fine particulate surfaces. Fine-particulate smectite clays in large abundances can display residual restrahlen bands near 1050 cm^{-1}, which are not present in the data presented here. This is consistent with the lack of evidence for sheet silicates from other remote sensing observations (e.g., Bell et al., 1996).

The presence of a plagioclase component in the Martian soil would indicate that a significant portion of the high-albedo surface has been mechanically, but not chemically weathered. This indicates that the source material for the Martian soil has not been completely altered and constituents, such as glasses and iron-bearing minerals, have been preferentially altered, leaving unaltered plagioclase as the only significant unaltered component.

This proposed mineralogy is similar to a particular thermally altered palagonitic tephra reported by Bell et al. (1993) as a Martian VNIR spectral analog. Though quantitative mineral abundances are difficult to determine with such materials, X-ray diffraction indicated that both coarse and fine grain size fractions of the tephra samples are dominated by plagioclase with minor amounts of pyroxene, smectite clay, and hematite (Bell et al., 1993). It has also been proposed that it is possible to preferentially alter other materials present on Mars and leave plagioclase as the only major unaltered phase (Gooding 1992). Though it is possible for plagioclase to be the most weathering resistant component in mafic mineral assemblages, reaction rates can vary significantly based on the conditions present.

An alternate explanation is that the Martian soil is a mixture of several source lithologies and the unaltered component may have a different source and weathering history as the clearly altered components. A separate plagioclase source without evidence of other primary minerals may be consistent with highly differentiated materials, such as anorthosites, but there is little evidence for these types of rocks on Mars from either remote sensing observations or the Martian meteorites (e.g., McSween 1994, Bell 1996, Christensen et al., 2001; Bandfield 2002).

Unfortunately, there is little spectral or chemical distinction between zeolites and unaltered plagioclase. Ruff (2002) indicates that the Martian moderate- and high-albedo surface spectra are consistent with this mineralogy, which forms in a variety of environments, including hydrothermal alteration of volcanic rocks. It is possible that zeolitic materials may be present in the Martian dust at some level. However, there are several arguments against their ubiquitous presence in the Martian dust in lieu of plagioclase. Zeolites commonly form in a variety of low-grade metamorphic environments bounded by clays in less intense alteration environments and K-feldspar in higher temperature and pressure environments. There is little spectroscopic evidence for large abundances of either K-feldspar or clay products on the Martian surface. Zeolite materials have been identified as products of palagonitization of basaltic tuff deposits; however, a number of other products are formed as well, including opal, calcite, and montmorillonite (Hay and Iijima 1968). The volume and extent of the Martian dust make it unlikely that zeolites could be so extensively produced without detection of other secondary minerals. In addition, though clays have been identified in low abun-

dances in Martian meteorites, no zeolites have been identified (Basu et al., 1998).

Though indirect arguments may be used to indicate that plagioclase is the dominant source of the spectral features present at 800 cm^{-1}, the chemical and spectral (including VNIR measurements (Cloutis 2001)) determinations are not unique. Additional measurement techniques will be required to unambiguously distinguish the two mineral types.

V. Conclusions

A thorough and robust method for separating the spectral signatures of the Martian surface and atmosphere has been developed and applied to multiple emission angle data returned from the MGS TES instrument. This work has presented the following:

- Correlated-*k* and index gas removal algorithms have been developed for CO_2 and H_2O and may be applied to all nadir-pointing TES data.
- The results have provided new and refined measurements of the spectral shapes of atmospheric dust, low-albedo surfaces, and intermediate- and high-albedo surfaces.
- Surface temperatures are 1–4 K warmer than the nominal TES processing that derives surface temperatures from the wavelength of the highest brightness temperature. The magnitude of the error is positively correlated with the 9 μm dust opacity.
- Dust opacities at 9 μm are $\sim$0.09 higher than TES database opacities calculated from nadir observations only.
- Low-albedo surfaces display absorptions consistent in both shape and depth with previous studies. These surfaces may be closely modeled using a combination of previously derived basalt, andesitic, and high-albedo surface spectral shapes.
- Low-albedo surfaces display no significant absorptions at $>$1300 cm^{-1}, indicating both the coarse particulate nature of the surface and the lack of significant amounts ($<$5%) of carbonate.
- Moderate to high-albedo surfaces have spectral shapes distinctive of fine particulate silicate materials. These spectral signatures are probably dominated by particle sizes of $\sim<$40 μm.
- Moderate thermal inertia and albedo surfaces have spectral signatures similar to clearly dust-mantled high-albedo surfaces, indicating that a significant amount of loose fine particulate material is present in addition to any indurated surfaces proposed previously.
- No single material can match the entire high-albedo surface spectrum. There are clear indications of a material that closely matches calcic plagioclase and an emission peak near 1620 cm^{-1} due to bound water.
- The lack of residual restrahlen silicate absorptions indicates that minerals such as olivine or pyroxene are not present in high-albedo surfaces at significant (but unknown) abundances.
- High-albedo surface results presented here are in agreement and complimentary to shorter wavelength observations.
- The Martian dust is composed of both primary and secondary minerals. Either chemical weathering has not completely altered its source material or the soil is a mixture of altered and unaltered sources.
- Further laboratory studies are needed to better establish detection limits and behavior of mineral mixtures of fine particulates in the thermal infrared portion of the spectrum.

Acknowledgments

The authors would like to thank John Pearl for valuable advice throughout the development of this work. Phil Christensen, Steve Ruff, and Vicky Hamilton provided useful discussions during the progress of this work. Thanks also to Mike Kraft for an informal review as well as constructive formal reviews by Janice Bishop and Mike Wolff. This work was supported by a grant to JLB from the National Research Council.

References

Arvidson, R., Guiness, E., Dale-Bannister, M., Adams, J., Smith, M., Christensen, P., Singer, R., 1989. Nature and distribution of surficial deposits in Chryse Planitia and vicinity. J. Geophys. Res. 94, 1573–1587.

Bandfield, J.L., 2002. Global mineral distributions on Mars. J. Geophys. Res. 107 doi: 10.1029/2001JE001510.

Bandfield, J.L., Christensen, P.R., Smith, M.D., 2000a. Spectral dataset factor analysis and end-member recovery: application to martian atmospheric particulates. J. Geophys. Res. 105, 9573–9588.

Bandfield, J.L., Hamilton, V.E., Christensen, P.R., 2000b. A global view of martian surface compositions from MGS-TES. Science 287, 1626–1630.

Basu, A., Schmitt, J., Crossey, L.J., 1998. An argument for zeolites in Mars rocks and an Earth analog. Proc. Lunar Planet. Sci. 29 [CD-ROM].

Bell, J.F., III, 1996. Iron, sulfate, carbonate, and hydrated minerals on Mars. In: Dyar, M.D., McCammon, C., Schaefer, M.W. (Eds.), Mineral Spectroscopy: A Tribute to Roger G. Burns. Special Publications, Geochem. Soc. pp. 359–380.

Bell, J.F., III, Crisp, D., 1993. Groundbased infrared spectroscopy of Mars in the near infrared: preliminary results. Icarus 104, 2–19.

Bell, J.F., III, McCord, T.B., Owensby, P.D., 1990. Observational evidence of crystalline iron oxides on Mars. J. Geophys. Res. 95, 14447–14461.

Bell, J.F., III, Morris, R.V., Adams, J.B., 1995. Thermally altered palagonitic tephra: a spectral and process analog to the soil and dust of Mars. J. Geophys. Res. 98, 3373–3385.

Bell, J.F., III, et al., 2000. Mineralogic and compositional properties of Martian soil and dust: results from Mars Pathfinder. J. Geophys. Res. 105, 1721–1755.

Bishop, J.L., Froschl, H., Mancinelli, R.L., 1998. Alteration products in volcanic soils and identification of exobiologically important weathering products on Mars using remote sensing. J. Geophys. Res. 103, 31457–31476.

Christensen, P.R., Harrison, S.T., 1993. Thermal infrared emission spectroscopy of natural surfaces: application to desert varnish coatings on rocks. J. Geophys. Res. 98 (B11), 19819–19834.

Christensen, P.R., Anderson, D.L., Chase, S.C., Clark, R.N., Kieffer, H.H., Malin, M.C., Pearl, J.C., Carpenter, J., Bandiera, N., Brown, F.G., Silverman, S., 1992. Thermal Emission Spectrometer experiment: Mars Observer Mission. J. Geophys. Res. 97, 7719–7734.

Christensen, P.R., Bandfield, J.L., Smith, M.D., Hamilton, V.E., Clark, R.N, 2000a. Identification of a basaltic component on the martian surface from Thermal Emission Spectrometer data. J. Geophys. Res. 105, 9609–9621.

Christensen, P.R., Bandfield, J.L., Clark, R.N., Edgett, K.S., Hamilton, V.E., Hoefen, T., Kieffer, H.H., Kuzmin, R.O., Lane, M.D., Malin, M.C., Morris, R.V., Pearl, J.C., Pearson, R., Roush, T.L., Ruff, S.W., Smith, M.D, 2000b. Detection of crystalline hematite mineralization on Mars by the Thermal Emission Spectrometer: evidence for near-surface water. J. Geophys. Res. 105, 9632–9642.

Christensen, P.R., Bandfield, J.L., Hamilton, V.E., Ruff, S.W., Kieffer, H.H., Titus, T.N., Malin, M.C., Morris, R.V., Lane, M.D., Clark, R.L., Jakosky, B.M., Mellon, M.T., Pearl, J.C., Conrath, B.J., Smith, M.D., Clancy, R.T., Kuzmin, R.O., Roush, T., Mehall, G.L., Gorelick, N., Bender, K., Murray, K., Dason, S., Greene, E., Silverman, S., Greenfield, M., 2001. The Mars Global Surveyor Thermal Emission Spectrometer experiment: investigation description and surface science results. J. Geophys. Res. 106, 23823–23871.

Clark, B.C., 1993. Geochemical components in martian soil. Geochim. Cosmochim. Acta 57, 4575–4582.

Clark, B.C., Baird, A.K., Weldon, R.J., Tsusaki, D.M., Schnabel, L., Candelaria, M.P., 1982. Chemical composition of martian fines. J. Geophys. Res. 87, 10059–10067.

Cloutis, E.A., Asher, P.M., Mertzman, S.A., Guertin, M, 2001. Spectral reflectance properties of zeolite group minerals. Proc. Lunar Planet. Sci. 32 [CD-ROM].

Conel, J.E., 1969. Infrared emissivities of silicates: experimental results and a cloudy atmosphere model of spectral emission from condensed particulate mediums. J. Geophys. Res. 74, 1614–1634.

Conrath, B.J., Pearl, J.C., Smith, M.D., Maguire, W.C., Dason, S., Kaelberer, M.S., Christensen, P.R, 2000. Mars Global Surveyor Thermal Emission Spectrometer (TES) observations: atmospheric temperatures during aerobraking and science phasing. J. Geophys. Res. 105, 9509–9519.

Cooper, C.D., Mustard, J.F., 1999. Effects of very fine particle size on reflectance spectra of smectite and palagonitic soil. Icarus 142, 557–570.

Cooper, C.D., Mustard, J.F, 2002. Spectroscopy of loose and cemented sulfate-bearing soils: implications for duricrust on Mars. Icarus 158, 42–550.

Foley, C.N., Economou, T.E., Clayton, R.N, 2001. Chemistry of Mars Pathfinder samples determined by the APXS. Proc. Lunar Planet. Sci. 32 [CD-ROM].

Gooding, J.L., 1992. Soil mineralogy and chemistry on Mars: possible clues from salts and clays in SNC meteorites. Icarus 99, 28–41.

Goody, R., Yung, Y.L., 1989. Atmospheric Radiation: Theoretical Basis. Oxford Univ. Press, New York.

Goody, R., West, R., Chen, L., Crisp, D., 1989. The correlated-*k* method for radiation calculations in nonhomogeneous atmospheres. J. Quant. Spect. Radiat. Transfer 42, 539–550.

Grove, C.I., Hook, S.J., Paylor, E.D., II, 1992. Laboratory Reflectance Spectra of 160 Minerals, 0.4 to 2.5 Micrometers, Publication 92–2. JPL.

Hay, R.L., Iijima, A., 1968. Petrology of palagonite tuffs of Koko Craters, Oahu, Hawaii. Contrib. Mineral. Petrol. 17, 141–154.

Hudson, N., Bonnet, B., Scott, N.A., Chedin, A., 1992. Management and study of spectroscopic information—The GEISA program. J. Quant. Spectrosc. Radiat. Transfer 48, 509–518.

Jakosky, B.M., Finiol, G.W., Henderson, B.G., 1990. Directional variations in thermal emission from geologic surfaces. Geophys. Res. Lett. 17, 985–988.

Kieffer, H.H., Martin, T.Z., Peterfreund, A.R., Jakosky, B.M., Miner, E.D., Palluconi, F.D., 1977. Thermal and albedo mapping of Mars during the Viking primary mission. J. Geophys. Res. 78, 4291–4312.

Lane, M.D., Christensen, P.R., 1998. Thermal infrared emission spectroscopy of salt minerals predicted for Mars. Icarus 135, 528–536.

Logan, L.M., Hunt, G.R., Salisbury, J.W., Balsamo, S.R., 1973. Compositional implications of Christiansen frequency maximums for infrared remote sensing applications. J. Geophys. Res. 78, 4983–5003.

McSween, H.Y., Jr., 1994. What have we learned about Mars from SNC meteorites. Meteoritics 29, 757–779.

Mellon, M.T., Jakosky, B.M., Kieffer, H.H., Christensen, P.R, 2000. High-resolution thermal inertia mapping from the Mars Global Surveyor Thermal Emission Spectrometer. Icarus 148, 437–455.

Morris, R.V., Agresti, D.G., Lauer, H.V., Jr., Newcomb, J.A., Shelfer, T.D., Murali, A.V., 1989. Evidence for pigmentary hematite on Mars based on optical, magnetic, and Mossbauer studies of super-paramagnetic (nanocrystalline) hematite. J. Geophys. Res. 94, 2760–2778.

Murchie, S., Mustard, J., Bishop, J., Head, J., Pieters, C., Erard, S., 1995. Spatial variations in the spectral properties of bright regions on Mars. Icarus 105, 454–468.

Pearl, J.C., Smith, M.D., Conrath, B.J., Bandfield, J.L., Christensen, P.R, 2001. Observations of martian ice clouds by the Mars Global Surveyor Thermal Emission Spectrometer: The First Martian Year. J. Geophys. Res. 106, 12325–12338.

Pimentel, G., Forney, P., Herr, K., 1974. Evidence about hydrate and solid water in the martian surface from the 1969 Mariner infrared spectrometer. J. Geophys. Res. 79, 1623–1634.

Ramsey, M.S., Christensen, P.R., 1998. Mineral abundance determination: quantitative deconvolution of thermal emission spectra. J. Geophys. Res. 103, 577–596.

Reider, R.T., Economou, T., Wanke, H., Turkevich, A., Crisp, J., Bruckner, J., Drebus, G., McSween, H.Y., Jr., 1997. The chemical composition of Martian soil and rocks returned by the mobile alpha proton X-ray spectrometer: preliminary results from the X-ray mode. Science 278, 1771–1774.

Roush, T.L., Bell, J.F., III, 1995. Thermal emission measurements 2000–400 cm^{-1} (5–25 μm) of Hawaiian palagonitic soils and their implications for Mars. J. Geophys. Res. 100, 5309–5317.

Ruff, S.W., 1998. Quantitative Thermal Infrared Emission Spectroscopy Applied to Granitoid Petrology. Ph.D. Thesis, Arizona State University.

Ruff, S.W., 2002. Spectral evidence for zeolite in the dust on Mars. Eos 83, (Spring Supplement) 1059.

Ruff, S.W., Christensen, P.R., 2002. Bright and dark regions on Mars: particle size and mineralogical characteristics based on Thermal Emission Spectrometer data. J. Geophys. Res., in press.

Ruff, S., Christensen, P.R., Barbera, P.W., Anderson, D.L., 1997. Quantitative thermal emission spectroscopy of minerals: a technique for measurement and calibration. J. Geophys. Res. 102, 14899–14913.

Ruff, S.W., Christensen, P.R., Clark, R.N., Malin, M.C., Bandfield, J.L., Lane, M.D., Mellon, M.T., Prestley, M.A., 2001. Mars' "White Rock" feature lacks evidence of an aqueous origin. J. Geophys. Res. 106, 23921–23927.

Salisbury, J.W., Walter, L.S., 1989. Thermal infrared (2.5–13.5 μm) spectroscopic remote sensing of igneous rock types on particulate planetary surfaces. J. Geophys Res. 94, 9192–9202.

Salisbury, J.W., Basu, A., Fischer, E.M., 1997. Thermal infrared spectra of lunar soils. Icarus 130, 125–139.

Smith, M.D., 2002. The annual cycle of water vapor on Mars as observed by the Thermal Emission Spectrometer. J. Geophys Res., in press.

Smith, M.D., Bandfield, J.L., Christensen, P.R., 2000a. Separation of atmospheric and surface spectral features in Mars Global Surveyor Thermal Emission Spectrometer (TES) spectra. J. Geophys. Res. 105, 9589–9607.

Smith, M.D., Pearl, J.C., Conrath, B.J., Christensen, P.R., 2000b. Mars Global Surveyor Thermal Emission Spectrometer (TES) observations of dust opacity during aerobraking and science phasing. J. Geophys. Res. 105, 9539–9552.

Smith, M.D., Pearl, J.C., Conrath, B.J., Christensen, P.R. 2002. Thermal Emission Spectrometer Observations of Martian planet encircling dust storm 2001a. Icarus, in press.

Snook, K.J., 2002. Properties of suspended Martian dust using MGS-TES data. Proc. Lunar Planet. Sci. 33 [CD-ROM].

Toon, O.B., Pollack, J.B., Sagan, C., 1977. Physical properties of the particles composing the martian dust storm of 1971–1972. Icarus 30, 663–696.

Toulmin, P., Baird, A.K., Clark, B.C., Keil, K., Rose, H.J., Christian, R.P., Evans, P.H., Kelliher, W.C., 1977. Geochemical and mineralogical interpretation of the Vikings inorganic chemical results. J. Geophys. Res. 82, 4625–4634.

Wolff, M.J., Clancy, R.T., Pitman, K.M., Christensen, P.R., Whitney, B.A., 2001. Mars aerosol studies with the MGS TES emission phase function Observations: opacities, particle sizes, and ice cloud types. Proc. Div. Planet. Sci. 33, 34.06.